Numerical and experimental study on high-speed hydrogen–oxygen combustion gas flow and aerodynamic heating characteristics

Cite as: Phys. Fluids **33**, 076103 (2021); https://doi.org/10.1063/5.0052919
Submitted: 02 April 2021 • Accepted: 31 May 2021 • Published Online: 02 July 2021

Jiangpeng Yu, Jinping Li, Qiu Wang, et al.

Physics of Fluids ARTICLE scitation.org/journal/phf

Numerical and experimental study on high-speed hydrogen–oxygen combustion gas flow and aerodynamic heating characteristics

Cite as: Phys. Fluids **33**, 076103 (2021); doi: 10.1063/5.0052919
Submitted: 2 April 2021 · Accepted: 31 May 2021 ·
Published Online: 2 July 2021

Jiangpeng Yu,[1,2] Jinping Li,[1,a)] Qiu Wang,[1] Shizhong Zhang,[1] and Xiaoyuan Zhang[1]

AFFILIATIONS

[1]State Key Laboratory of High Temperature Gas Dynamics, Institute of Mechanics, CAS, No.15 Beisihuanxi Road, Beijing 100190, China
[2]School of Engineering Science, University of Chinese Academy of Sciences, Beijing 100049, China

Note: This paper is part of the special topic, Selected Papers from the 11th National Congress on Fluid Mechanics of China.
[a)]**Author to whom correspondence should be addressed:** lijinping@imech.ac.cn

ABSTRACT

The need to increase the payload capacity of the rockets motivates the development of high-power rocket engines. For a chemical propulsion system, this results in an increasing thermal load on the structure, especially the combustion chamber and nozzle must be able to withstand the extreme thermal load caused by high-temperature and high-pressure combustion gas. In order to protect the structure from the effect of increasing heat flux, it is necessary to counteract such effect with more advanced thermal management technology. This requires us to accurately predict the aerodynamic heating of the structure by high-temperature and high-speed combustion gas. In this study, a high-temperature combustion gas tunnel developed in the laboratory is used to produce high-speed combustion gas. Combined with the results of numerical calculation, the flow and aerodynamic heating characteristics of air and hydrogen–oxygen combustion gas under the same total temperature and pressure are analyzed and compared. The comparison revealed that the combustion gas flow in the nozzle has higher static temperature, velocity, and smaller Mach number. When the combustion gas flows around the sphere, the shock standoff distance and stagnation pressure are smaller than those of air, and the wall heat flux is much larger than that of air. The active chemical reaction in the combustion gas makes the aerodynamic heating of the structure more severe. Finally, through the analysis of a large amount of data, a semi-empirical formula for the heat flux of the stagnation point heated by a high-speed hydrogen and oxygen equivalent ratio combustion gas is obtained.

I. INTRODUCTION

With the development of aeronautics and spaceflight, higher requirements are proposed for the payload capacity of rockets. Increasing the combustion temperature and pressure in the chamber contributes to the achievement of higher specific impulse and increases the compactness of the chamber, which are the main means to improve the performance of the engine.[1] However, the combustion chamber and nozzle in the rocket engine will bear a great thermal load. In the high-speed flow where the adiabatic temperature in the combustion chamber exceeds 3500 K, the extreme heat flow in the nozzle can reach 150 MW/m^2.[2] Moreover, increasing the combustion pressure and temperature of the chamber will directly lead to an increase in heat flux, since the heat flux is approximately linearly proportional to the chamber pressure: $Qw \sim P^{0.8}$.[3] The huge thermal load reduces the structural strength and increases the risk of damage, which restricts the development of high-performance engines. This requires more rigorous thermal protection design of all the components of the engine, and the cooling system must be able to efficiently transfer heat from the engine walls. An excessively small redundancy of the cooling system will compromise the safety of the spacecraft, while a too large redundancy will increase the load and reduce the payload of the rocket. A reasonable design of the cooling system requires accurate prediction of the thermal load, that is, the heat flux of aerodynamic heating of the chamber and nozzle by high-temperature and high-speed combustion gas.[4–6]

Currently, the research on the heat flux of the chamber and nozzle is mainly conducted through rocket engine combustion experiments and numerical calculations. The methods of heat flux measurement mainly include calorimetric method, inverse heat transfer method, etc. The calorimetric method assumes that the cooled

structure is in thermal equilibrium, and then the heat flux entering the structure is equal to the heat flux entering the cooling medium, thereby indirectly measuring the heat flux on the wall of the rocket structure. Since this method ignores the natural convection on the outer walls of the structure, there is a certain error, and the result is usually the average result of a certain cooling area, so the spatial resolution is generally low.[6,7] The inverse heat transfer method is based on the inverse solution of the heat conduction problem, by optimizing the program to estimate the measuring temperature with the experiment, to obtain the best match of the value of the unknown boundary conditions, but since the inverse heat transfer problems are a known class of ill-posed problems, there are no unique solutions.[8–12] As a result, since most of the combustor and nozzle materials do not have constant heat transfer characteristics, there are some errors in the results of the inverse heat transfer method. In addition to certain limitations of the measurement methods, rocket engine tests are costly and have strong relevance for the specific gas, model, and material tests, so their conclusions are difficult to be generalized.[13–15] Currently, there are a few quantitative experimental studies on high-temperature high-speed combustion gas flow and aerodynamic heating. Computational fluid dynamics (CFD) plays an important role in the early stages of the design of rocket engines. However, due to the complexity of combustion in rocket engines, involving turbulence, numerous elementary reactions, complex cavity models, mixing, etc., the computational efficiency is rather low. Therefore, researchers need to reduce the complexity of numerical calculation by simplifying the combustion process,[16] such as by laminar flamelet and frozen flamelet methods[17] and Probability Density Function (PDF) integration algorithm.[18] This directly accelerates the calculation but at the same time introduces certain errors. Therefore, relatively accurate quantitative experiments are needed to assist the results of numerical calculation and improve the accuracy of prediction.

Compared with air, combustion gas has more components, a lower activation energy of the reaction, and more drastic changes in components. Its thermodynamic characteristics and transport characteristics are far more complex than those of air, so it is difficult to generate high-speed flow of combustion gas at a specific state (temperature, pressure, and components). To this end, the JF-14 high-temperature combustion gas tunnel was developed through debugging at the Chinese Academy of Sciences Institute of Mechanics State Key Laboratory of High Temperature Gas Dynamics. The JF-14 can produce a high-temperature gas total temperature of 2000 to 4500 K, which is within the scope of different types of fuel (hydrogen, hydrocarbon, etc.) of the high-speed combustion gas, and the flow field uniform stability with long enough test time can meet the needs of quantitative experiments. Due to the advantages of clean combustion and large specific impulse, liquid hydrogen is often used in core boosters[19,20] and is one of the most widely used fuels for liquid rocket engines. Therefore, in this study, the JF-14 is used to conduct experimental research on the flow and aerodynamic heating characteristics of high-temperature and high-speed hydrogen–oxygen combustion gas. The flow in the rocket combustion chamber involves multiple physical processes, such as mixing and combustion, which are pretty complex. This paper focuses on the basic study of high-speed hydrogen–oxygen combustion gas flow and aerodynamic heating, so a simple model can help us to study the major problems. Due to the high-speed gas flow around the sphere, only the windward forms a bow shock, and there is a peak heat flux at the stagnation point, which provides important reference for the thermal/structural design of the engine. Accordingly, in this paper, the flow and aerodynamic heating characteristics of high-temperature and high-speed hydrogen–oxygen combustion gas are studied by measuring the heat flux at the stagnation point of the sphere and its vicinity, in combination with CFD. At present, there are many studies on the aerodynamic heating of the sphere by high enthalpy air, with abundant achievements related to its flow and heating characteristics.[21–24] The relevant conclusions are mature and reliable. In order to facilitate the understanding of the flow and heating characteristics of the hydrogen–oxygen combustion gas, the calculation and test results of the hydrogen–oxygen combustion gas in this study are compared with those of the air under the same total temperature and pressure.

II. RESEARCH METHODS

A. Experiment

The JF-14 high-temperature combustion gas tunnel, which is based on the backward-running detonation driving technique, its structure, and wave diagram, is shown in Fig. 1. It consists of a driving tube of 15 m in length, a driven tube of 11 m in length with an attached axisymmetric Laval nozzle, a vacuum tank, and a 3-m long damping section. The inner diameter of the driving and driven tubes amounts to 224 mm. A premixed hydrogen–oxygen–nitrogen explosive gas is filled into the evacuated driving tube and ignited with a 520-V electric spark close to a 1-mm thick steel main diaphragm, which separates the driving and driven tubes. Then, after an experimental gas is filled into the evacuated driven tube and the pressure of the gas in the driving tube jump across the detonation wave causes a fast rupture of the main diaphragm, the high-pressure gas enters the driven tube and forms an incident detonation wave. When the incident detonation wave ruptures the second diaphragm separating the driven section and nozzle, a shock wave is simultaneously reflected, which further compresses and stagnates the detonation products in the driven tube, forming the high-temperature and high-pressure combustion gas in the nozzle inlet. As the diaphragm ruptures, a quasi-steady nozzle flow is established after a short starting transient.[25] The structure of a high-temperature combustion gas tunnel is the same as that of a shock tunnel, and the only difference is that a shock tunnel generates high-temperature and high-pressure air through an incident shock wave and reflects a shock wave compression,[26–28] while a combustion gas tunnel generates test gas through an incident detonation wave and reflects a shock wave compression.

The high-pressure and high-temperature combustion gas of the JF-14 is produced by a detonation wave and a reflected shock wave and the principle is different from that of the shock tunnel. The moving detonation gas in the driving tube provides a moving boundary condition to weaken the expansion wave generated after the incident detonation wave in the driven tube. When the expansion wave generated after the detonation wave is completely eliminated, the high-temperature combustion gas tunnel is in a critical running state.[25] For this case, the gas in zone 2 is in the state of Chapman-Jouguet (CJ) point, which can be determined by the initial state and the detonation velocity of the mixture,

$$p_2 = p_{CJ} = \frac{\rho_1 V_{CJ}^2}{\gamma_D + 1}, \tag{1}$$

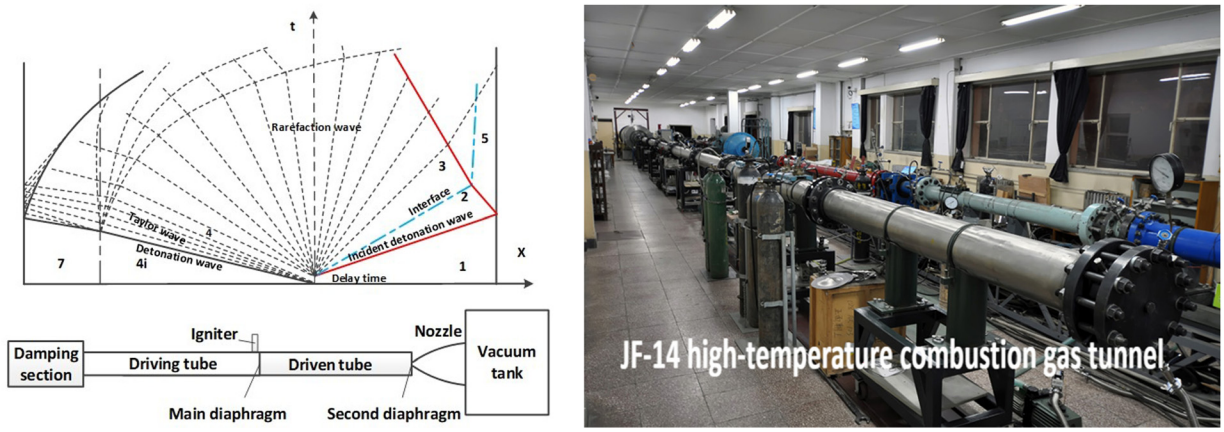

FIG. 1. Schematic diagram of the high temperature combustion gas tunnel structure.

$$u_2 = u_{CJ} = \frac{V_{CJ}}{\gamma_D + 1}, \tag{2}$$

$$a_2 = a_{CJ} = \frac{\gamma_D V_{CJ}}{\gamma_D + 1}. \tag{3}$$

Then, by the moving shock wave relation, it is obtained that[29]

$$\frac{u_2 - u_5}{a_2} = \frac{2}{\gamma_2 + 1}\left(Ma_{DR} - \frac{1}{Ma_{DR}}\right), \tag{4}$$

$$Ma_{DR} = \frac{u_2 - V_r}{a_2}, u_5 = 0, \tag{5}$$

where V_r is the velocity of the reflected shock wave.

The state parameters of zone 5 can be obtained from the above variables,

$$\frac{P_5}{P_2} = 1 + \frac{2\gamma_2}{\gamma_2 + 1}(Ma_{DR}^2 - 1), \tag{6}$$

$$\left(\frac{a_5}{a_2}\right)^2 = \frac{\left(\frac{2\gamma_2}{\gamma_2+1}Ma_{DR}^2 - \frac{\gamma_2 - 1}{\gamma_2 + 1}\right)\left(1 + \frac{\gamma_2 - 1}{2}Ma_{DR}^2\right)}{\frac{\gamma_2 + 1}{2}Ma_{DR}^2}. \tag{7}$$

B. Numerical calculation

In order to describe the parameter distribution of the flow field in more detail, numerical calculation was performed for the experiment due to the limited information obtained by the experimental measurement approach. The two-dimensional axisymmetric compressible Navier–Stokes (N–S) equation and the total-variation-diminishing (TVD) shock capturing scheme are used in the calculation. For air flow and aerodynamic heating, the chemical nonequilibrium reaction model of seven-components (O_2, N_2, O, N, NO, e^-, and NO^+) is used. For combustion gas, a nine-component (H_2O, O_2, H_2, N_2, OH, H, O, H_2O_2, and HO_2) chemical nonequilibrium reaction model is used. The thermodynamic parameters were fitted using the McBride polynomial, and the viscosity coefficient was fitted by the Sutherland–Wilke equation.

Considering that the nozzle is a rotating body, the calculation area of 1/2 cross section can maintain the accuracy while improving the calculation efficiency. The number of nozzle mesh grids is 1200×100, and the normal size of the grids near the wall is 1.0×10^{-5} m. A sphere with a radius of 20 mm was used in the experiment. Considering that the sphere is a three-dimensional rotating body, the calculation model can be simplified to a 1/4 circle, the number of mesh grids is 313×300, the wall normal mesh grid size is 1.0×10^{-6} m (the Reynolds number of the wall mesh grids is less than 20, which meets the heat flux calculation requirements), and the wall is orthogonal to the near-wall mesh. The wall boundary conditions are nonslip constant temperature wall (T = 300.0 K).

Under the test conditions, the chamber pressure is about 15 atm, the temperature is about 3500 K, and the characteristic length of the nozzle is 0.3 m (outlet diameter). According to the isentropic expansion relationship of the nozzle [Eqs. (8)], the Re of the nozzle flow is calculated to be about 1.03×10^5, so the Spalart–Allmaras turbulence model is used for the nozzle flow. The Re of the flow around the sphere is about 8.26×10^3, so the laminar model is used for the flow around the sphere,

$$\frac{\sigma_e}{\sigma^*} = \frac{1}{Ma_e}\left[\frac{2}{\gamma + 1}\left(1 + \frac{\gamma - 1}{2}Ma_e^2\right)\right]^{\frac{\gamma+1}{2(\gamma-1)}}, \tag{8a}$$

$$T = \frac{T_0}{1 + \frac{\gamma - 1}{2}Ma_e^2}, \quad P = \frac{P_0}{\left(1 + \frac{\gamma - 1}{2}Ma_e^2\right)^{\frac{\gamma}{\gamma-1}}}. \tag{8b}$$

III. EXPERIMENTAL RESULTS AND ANALYSES

A. The pitot pressure distribution in test section

In the ideal experiment, the high-speed gas flow field from the nozzle remains uniform and stable during the effective time. However, due to the complexity of the flow in the Laval nozzle, the actual state of the flow field may be different from that of the design, so the flow field should be tested before the experiment.

In this experiment, the uniformity of the flow field was tested by measuring the pitot pressure in different areas at the nozzle outlet. A

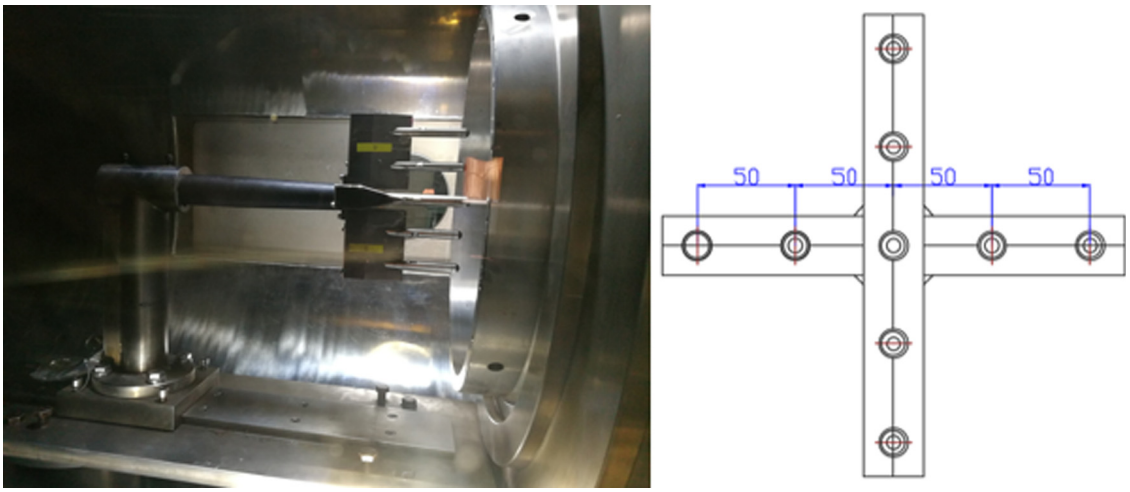

FIG. 2. Pitot harrow (left) and sensor distribution (right).

TABLE I. Inflating parameters of the high-temperature combustion gas tunnel.

	Deriving tube	P_4/MPa	T_4/K	Driven tube	P_1/KPa	T_1/K	P_5/MPa	T_5/K
Case 1	$2H_2 + O_2 + 1.6N_2$	0.3	298	$2H_2 + O_2 + 3.76N_2$	41	298	1.475	3211
Case 2	$2H_2 + O_2 + 0.5N_2$	0.3	298	$2H_2 + O_2 + 1.6N_2$	40	298	1.6	3501
Case 3	$3H_2 + O_2$	0.3	298	$2H_2 + O_2$	30.2	298	1.55	3838

pitot harrow, as shown in Fig. 2, was used for the experiment. The pitot harrow is fitted with nine SN-3 piezoresistive sensors, each 50 mm apart, facing and attached to the nozzle outlet.

The above tunnel and pitot harrow are used to test the quality of the flow field of the high-temperature combustion gas tunnel. The inflation parameters of the driving and driven tubes of different cases are listed in Table I. The reservoir region pressure values of case 1, case 2, and case 3 were measured at 1.475, 1.6, and 1.55 MPa, respectively. Based on the detonation wave velocity and the initial components of the driven section, the total temperature values were calculated as 3211, 3501, and 3838 K, respectively, through the equilibrium chemical reaction.[30] The reservoir region pressure curves of the three cases are shown in Fig. 3, and the effective test times are all greater than 10 ms.

The outlet diameter of the nozzle used in the experiment is 300 mm, the throat diameter is 30 mm, and the expansion ratio is 100. The nozzle nominal Mach number for air is 6. The test pressure traces from each of the sensors and calculated results of the pitot pressure at the nozzle outlet are shown in Figs. 4(a)–4(c). These results reveal that the pitot pressure at the nozzle outlet is evenly distributed, and the measured value is basically consistent with the numerical calculation.

Through the analysis of the pitot pressure, the combustion gas flow field of the different cases is uniformly and stably distributed within the measurement range, and the test time is more than 10 ms, which meets the experimental requirements. Moreover, the experimental data and the numerical calculation results are very consistent, indicating that the high-speed combustion gas generated by the high-temperature combustion gas tunnel is consistent with the expectation. The detailed nozzle exit data are shown in Table II.

B. Heat flux at the stagnation point and nearby

In this experiment, three stainless-steel spheres with a radius of 20 mm, as shown in Fig. 5 (left), are used, and five E-type coaxial

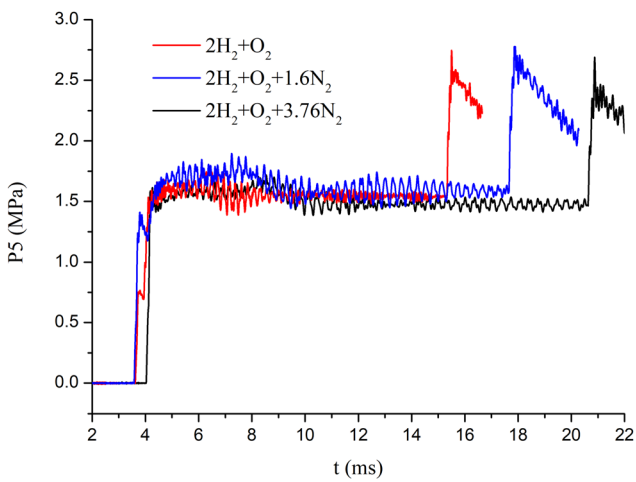

FIG. 3. Reservoir region pressure curves.

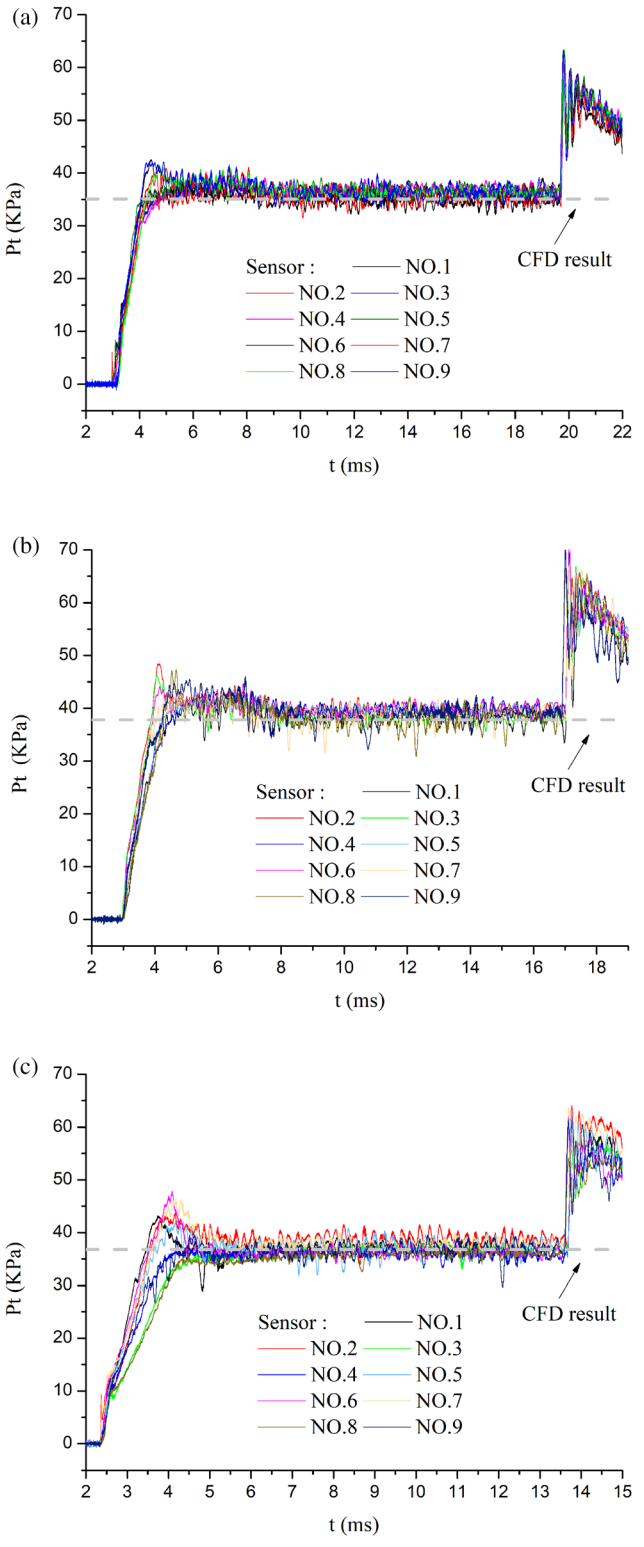

FIG. 4. The pitot pressure traces for the different cases. (a) $2H_2 + O_2 + 3.76N_2$, (b) $2H_2 + O_2 + 1.6N_2$, and (c) $2H_2 + O_2$.

TABLE II. Nozzle outlet parameters.

Sort	P (Pa)	T (K)	U (m/s)	M
Case 1	1065	769	3045	5.1
Case 2	1355	1142	3551	4.7
Case 3	1475	1503	4679	4.5

thermocouple heat flux sensors are installed on the surface of each sphere at an interval of 15°. The three spheres are installed side by side in the horizontal direction of the pitot harrow, at an interval of 100 mm from each other, and the front end of the sphere is flushed with the nozzle outlet. The field installation is shown in Fig. 5 (right).

The test was conducted according to the inflation parameters shown in Table I and the typical heat flux curve is shown in Fig. 6. Influenced by the starting waves of the nozzle, the heat flux data tended to be stable after experiencing drastic changes.

As shown in Fig. 7, the supersonic flow forms a bow shock wave on the upwind side of the sphere, thereby compressing and slowing down the gas. The temperature and pressure rise rapidly across the shock wave, and a large temperature gradient is formed near the wall surface. Driven by the temperature gradient, the thermal is conducted to the wall. The high temperature environment after the shock wave shifts the chemical reaction in the endothermic direction, which leads directly to the decomposition of combustion products (H_2O), and the gas, driven by the concentration gradient, diffuses toward the wall. There are three wall conditions: noncatalytic wall, finite catalytic wall, and catalytic wall. When the wall surface is noncatalytic, the composition of the wall surface is determined by the rate of the nonequilibrium chemical reaction, and the wall heat flux is usually the minimum. When the wall surface is completely catalyzed, the chemical reaction reaches equilibrium instantly at the wall surface, that is, the products decomposed due to the high temperature after the shock wave quickly compounds on the wall surface and releases a large amount of thermal, at which time the heat flux reaches the maximum. The finitely catalyzed wall heat flux condition is between the two.

Heat flux sensors on the sphere are installed at both sides at 0°, 15°, and 30°, as shown in Fig. 5. Through the analysis of the test results and comparison with the numerical results under different wall conditions, it is found that the measured heat flow value of the hydrogen–oxygen combustion gas is close to the result of the completely catalyzed wall, and the error between the average measured heat flux of the four tests and that calculated under the condition of complete catalytic wall is about 5%. The test results confirm the accuracy of numerical calculation. The results also reveal that the stainless-steel material has a significant catalytic effect on the hydrogen–oxygen combustion gas, as shown in Figs. 8(a)–8(c).

IV. FLOW AND AERODYNAMIC HEATING CHARACTERISTICS OF HYDROGEN AND OXYGEN COMBUSTION GAS

As a result of the great differences in chemical reactions of the different combustion gases, it is very difficult to generate high-speed flow at the same total temperature and pressure in the test. In order to intuitively compare the flow and aerodynamic heating characteristics of different combustion gases, the flow in the nozzle and wall heat flux

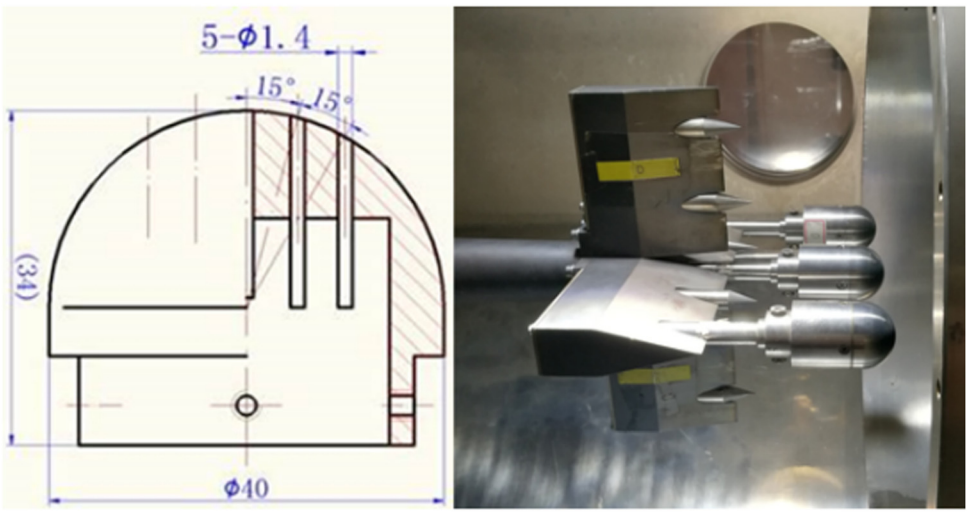

FIG. 5. Sensor distribution (left) and spheres (right).

of the sphere aerodynamically heated by different combustion gases at the same total temperature and pressure are calculated. The nonequilibrium chemical reaction model is used to calculate the flow in the nozzle of different gases at a total pressure of 15.5 atm and a total temperature of 3838 K. The outlet parameters of the nozzle are listed in Table III.

The gas expands in the nozzle, resulting in a rapid drop in temperature, shifting the chemical reaction in the exothermic direction, that is, the reaction producing water. When the molar ratios of H_2, O_2, and N_2 were 2:1:3.76, 2:1:1.6, and 2:1:0, the mass fraction of H_2O increased by 7.6%, 11.5%, and 20.3%, respectively, as the gas flowed through the nozzle. In contrast, when air at the same total temperature and pressure flows in the same nozzle, the O_2 mass fraction only increases by 4.7%. The mass fraction of O_2 in the air and H_2O in the combustion gas on the axis of the nozzle is shown in Fig. 9, which also

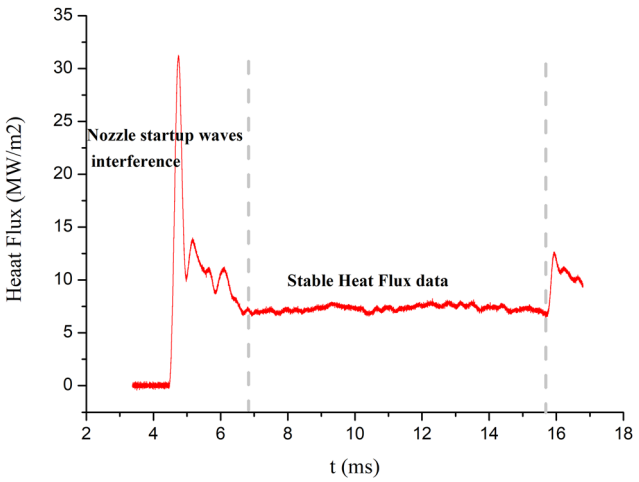

FIG. 6. Typical test heat flux curve.

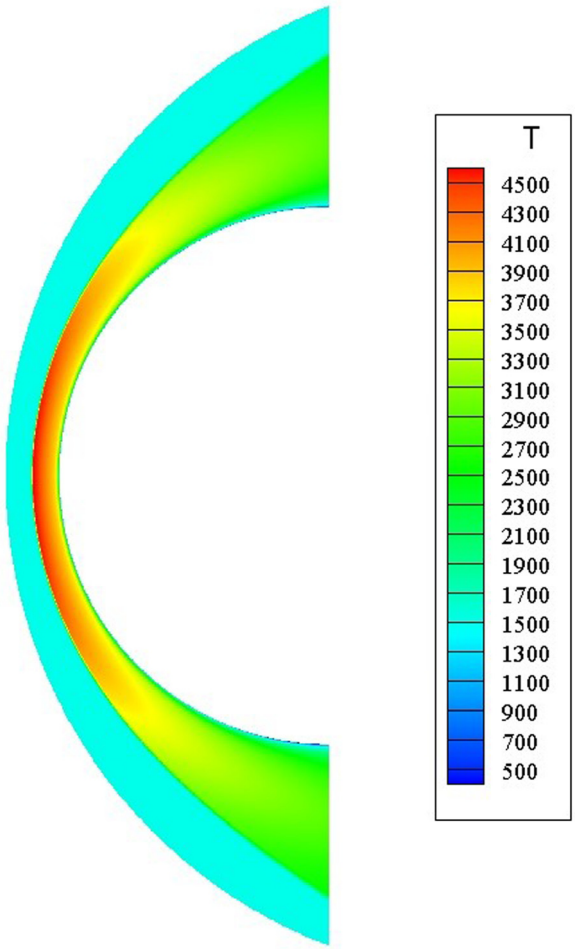

FIG. 7. Temperature contour.

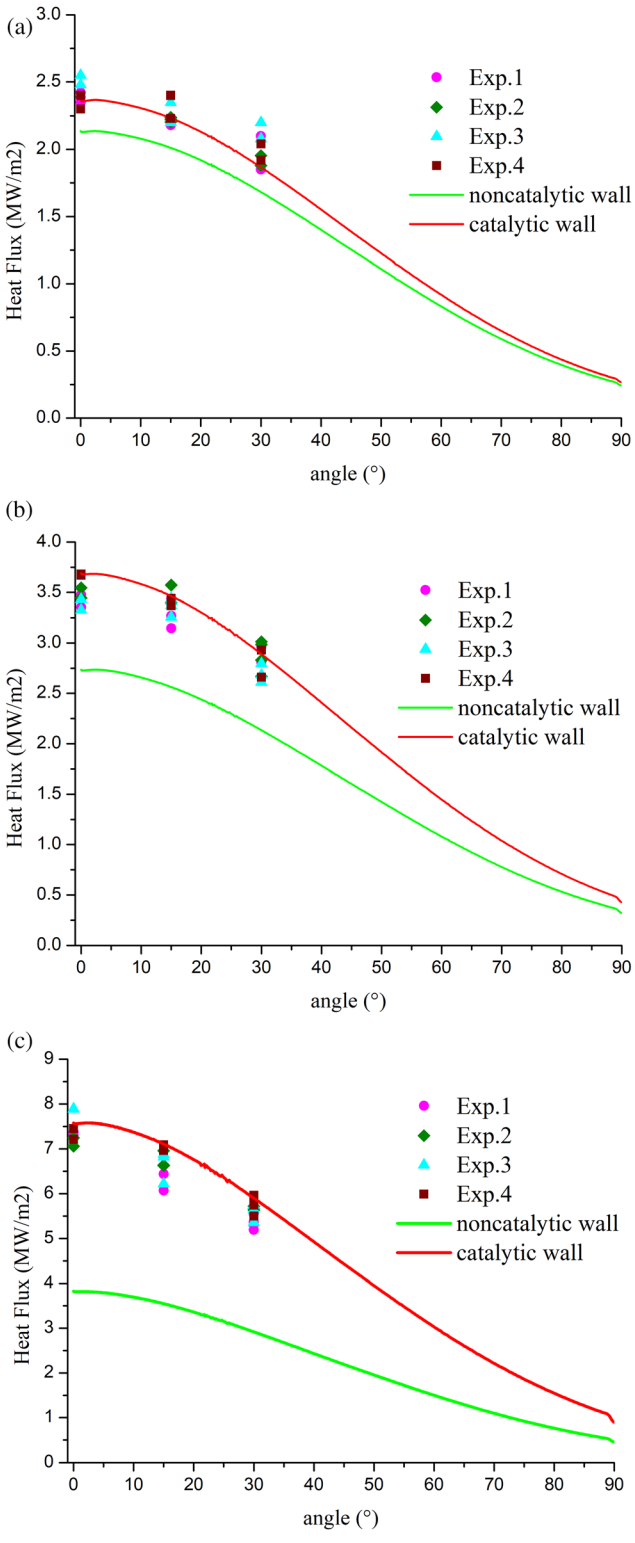

FIG. 8. The wall heat flux distribution for the different cases. (a) $2H_2 + O_2 + 3.76N_2$, (b) $2H_2 + O_2 + 1.6N_2$, and (c) $2H_2 + O_2$.

TABLE III. The nozzle outlet parameters.

Gases	P (Pa)	T (K)	U (m/s)	M
Air	866	727	2985	5.5
$2H_2 + O_2 + 3.76N_2$	1195	1073	3589	4.9
$2H_2 + O_2 + 1.6N_2$	1294	1240	3923	4.7
$2H_2 + O_2$	1475	1503	4679	4.5

reveals that the mass fraction of the components does not change in the process of air flow in the expanding section of the nozzle and is in a frozen state. In the process of the combustion gas flow in the expanding section of the nozzle, the components still change slightly, the flow is just close to the frozen state, and with the increase in the H_2 and O_2 content, the expanding section gradually shifts away from the frozen state. When different gases at the same total temperature and pressure flow through the nozzle, since the combustion gas products react and release more heat, the combustion gas has a higher temperature and speed, and this trend is made more obvious by the increase in the H_2 and O_2 content.

The outlet parameters of the aforementioned gas at the same total temperature (3838 K) and pressure (15.5 atm) flowing out of the Laval nozzle were taken as the boundary conditions, and the flow around the sphere with a radius of 20 mm was calculated. In order to compare the effects of chemical reactions on the flow, the freezing chemical reaction and nonequilibrium chemical reaction models were used, respectively. The results show that the shock standoff distance decreases with the increase in the H_2 and O_2 content in both models. Compared with the flow of the frozen chemical reaction, the shock standoff distance calculated by the nonequilibrium chemical reaction model is smaller, and this phenomenon is more obvious in high-speed combustion gas than in air. When the flow is air, the disintegration of the gas after the shock wave reduces the shock standoff distance by 0.8%, while when the flow is the combustion gas with H_2 and O_2 equivalent ratio, it decreases by more than 10%, as shown in Table IV. The temperature variation of the stagnation line is shown in Fig. 10, in

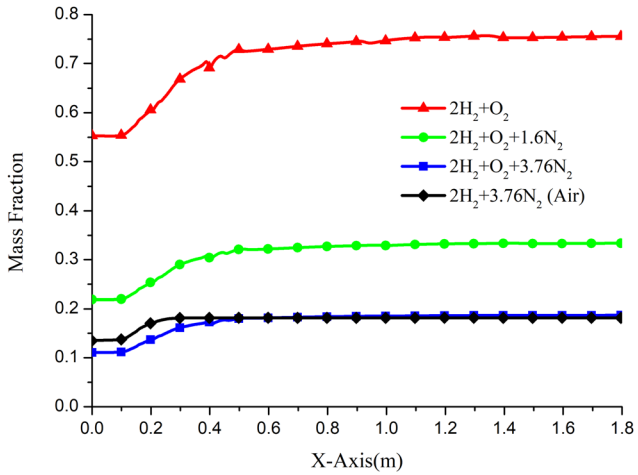

FIG. 9. Variation of the nozzle axis components.

TABLE IV. Shock standoff distances of different gases unit: mm.

Component	Frozen reaction	Nonequilibrium	Variation
Air	2.52	2.5	−0.8%
$2H_2 + O_2 + 3.76N_2$	2.28	2.42	−5.7%
$2H_2 + O_2 + 1.6N_2$	2.37	2.17	−8.44%
$2H_2 + O_2$	2.26	2.03	−10.18%

which this phenomenon can be observed intuitively. Since the temperature rises rapidly after the shock wave, the reaction shifts in the endothermic direction, and the H_2O in the combustion gas is endothermic and decomposes, thus reducing the temperature. However, the chemical reaction has little effect on the pressure, leading to the increase in the gas density after the shock wave, which further leads to a decrease in the shock wave standoff distance. When the flow is air, the temperature rises after the shock wave and O_2 begins to dissociate. However, only a small part of the O_2 begins to dissociate under this temperature condition. Therefore, the effect of chemical reactions in the air on the shock standoff distance is insignificant.

The thermal conductivity coefficient of the gas is related to its composition and temperature. With an increase in the H_2 and O_2 content, the thermal conductivity coefficient of the gas increases and is much larger than that of air, as shown in Fig. 11. Compared with the calculation results of the freezing chemical reaction, the decomposition of H_2O after the shock waves in the chemical nonequilibrium model concurrently reduces the thermal conductivity coefficient and the temperature, leading to a decrease in the temperature gradient near the wall. When the wall catalysis is not taken into account, the decrease in the temperature gradient directly leads to a decrease in the heat flux on the wall. When the flow is air, the O_2 is not completely dissociated when the condition of the total temperature is less than 4000 K, so the temperature change caused by the gas dissociation after the shock wave is very small, and the chemical reaction has little influence on the heat flux. The dissociation of the combustion gas after the shock waves reduces the temperature and thermal conductivity coefficient, so that

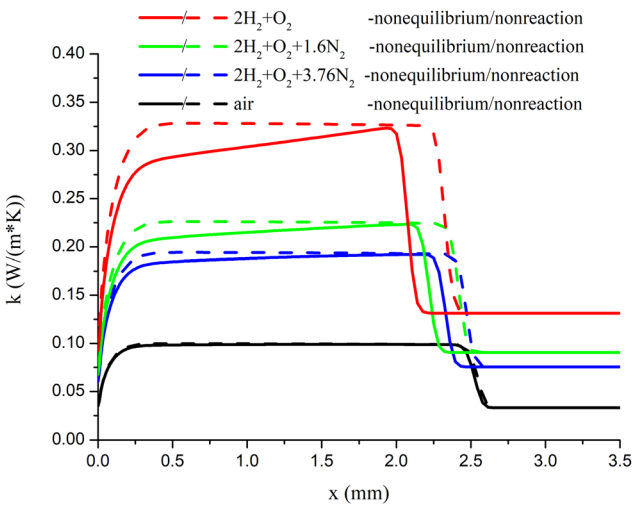

FIG. 11. Distribution of the thermal conductivity coefficient in the stagnation line (x: distance from the stagnation point).

the wall heat flux calculated by the nonequilibrium chemical model is about 14% smaller than that of the frozen chemical reaction model, while that of air shows little difference, as shown in Fig. 12. This indicates that the chemical reaction has a great influence on the combustion gas aerodynamic heating.

For the noncatalytic wall, the active chemical reactions in the combustion gas can reduce the heat flux, but as the experimental results reveal, the stainless-steel materials show complete catalytic performance for H_2 and O_2 combustion gas. Therefore, it is necessary to study the wall heat flux under the assumption of complete catalytic wall to provide the maximum possible heat flux for the cooling system design. The analysis of the numerical results shows that the wall heat flux increases sharply under the completely catalyzed wall hypothesis. The heat flux distribution on the surface of the sphere is shown in Fig. 13, and the heat flux at the stagnation point of the catalyzed/

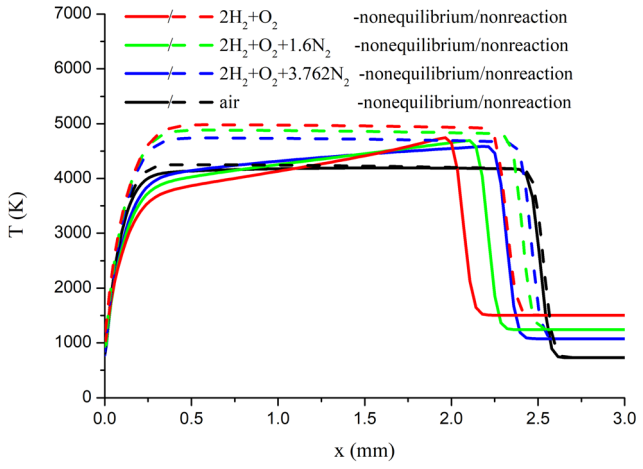

FIG. 10. Temperature distribution of the stationary line of the R20 sphere (x: distance from stagnation point).

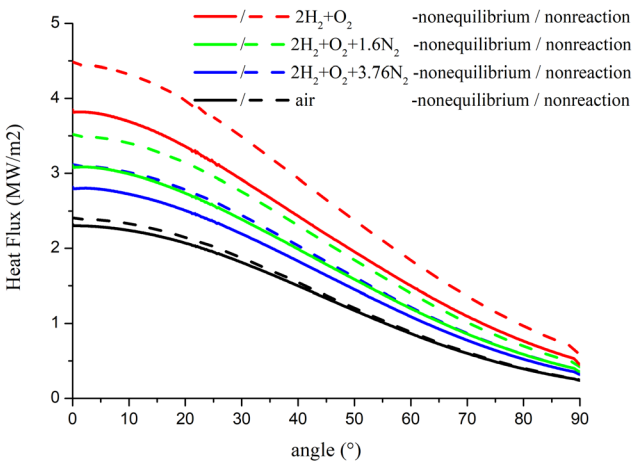

FIG. 12. Heat flux distribution on the surface of the R20 sphere (nonequilibrium and nonreaction).

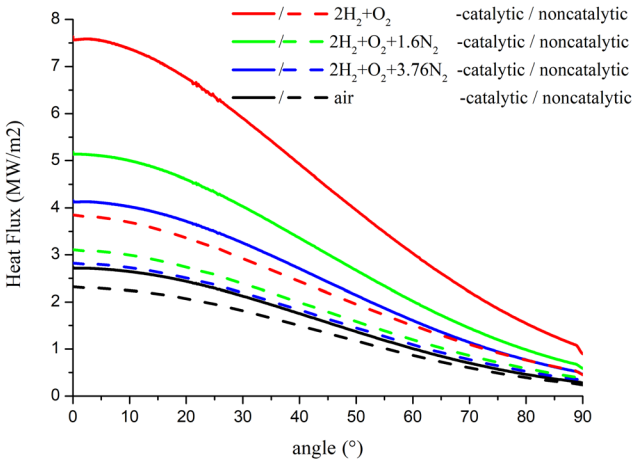

FIG. 13. Heat flux distribution on the surface of the R20 sphere (catalytic and noncatalytic wall).

noncatalyzed wall of a different gas is shown in Table V. Under the same total temperature and pressure, the heat flux at the stagnation point of aerodynamic heating by the H_2–O_2–N_2 combustion gas is much larger than that of air. For the equivalent ratio of H_2 and O_2, the heat flux at the completely catalyzed wall is nearly twice as large as that at the completely noncatalyzed wall, indicating that the higher the H_2 and O_2 content in the gas, the greater the influence of the wall catalytic conditions on the aerodynamic heating of the combustion gas.

The essential difference between air and the combustion gas is the composition. Under the high-temperature environment, the dissociation reaction of O_2 and N_2 occurs in the air, while in the combustion gas the decomposition reaction of H_2O occurs. Since the activation energy of the H_2O decomposition reaction is lower, the reaction is more likely to occur, and, besides, there is a large amount of H_2O in the gas after combustion. Although the temperature and pressure of the H_2 and O_2 combustion gas in the reservoir region are the same as those of air, the gas in the chemical equilibrium state contains more chemical energy, and the chemical energy is released as the combustion products react in the flow of the nozzle, so the combustion gas at the nozzle outlet has a higher temperature, pressure, and speed. In addition, the combustion gas is sensitive to the catalytic performance of the materials. Most metal materials and some metal oxide materials exhibit complete catalytic performance to the components of hydrogen and oxygen gas. The active chemical reactions in gas make the aerodynamic heating of the combustion gas more severely than that of air.

The common metal materials show catalytic properties for H_2 and O_2 combustion gas. In the case of ignoring radiation, the surface

TABLE V. Heat flux at the stagnation point unit: MW/m^2.

Gas/heat flux	Noncatalytic	Catalytic	Variation
Air	2.3	2.71	+17.8%
$2H_2 + O_2 + 3.76N_2$	2.82	4.16	+47.5%
$2H_2 + O_2 + 1.6N_2$	3.11	5.19	+66.7%
$2H_2 + O_2$	3.85	7.63	+98.2%

heat flux in the chemically reacting viscous flow of high-temperature and high-speed combustion gas is caused by thermal conduction and diffusion. The conduction heat flux is the thermal conduction driven by the temperature gradient, which can be calculated by the Fourier thermal conduction theory. The diffusion heat flux means that the dissociated gas diffuses to the wall under the drive of the component concentration gradient, and the chemical energy is brought to the wall through the compound reaction. Under the condition of complete catalysis of the wall, the gas components reach equilibrium state, the combustion products are completely compounded, and a large amount of heat of formation is released,

$$q_w = \left(k\frac{\partial T}{\partial y}\right)_w + \left(\rho D_{12}\sum_i h_i \frac{\partial c_i}{\partial y}\right)_w. \quad (9)$$

By decomposing the heat flux into conduction heat flux and diffusion heat flux, we can see the contribution of the chemical reaction to the heat flux under the condition of completely catalyzed wall. Through a large number of calculations of the gas in the total temperature range of 3000–5500 K, the change of the proportion of diffusion heat flux with the total temperature is summarized in Fig. 14. These results reveal that with an increase in the total temperature, the proportion of diffusion heat flux gradually increases, and when the total temperature remains constant, the proportion of diffusion heat flux also increases with an increase in the H_2 and O_2 content. This is due to the dissociation of more gas at higher temperatures. In this example, when the total temperature is 3800 K, the mass fraction of H_2O in the combustion gas after the shock wave decreases by about 16%, while when the total temperature rises to 4900 K, 44% of H_2O dissociates. Additionally, as the temperature increases, the degree of H_2O dissociation still increases. In contrast, the change in the mass fraction of O_2 in air is similar to the change in the percentage of water at the corresponding temperature. However, due to the high content of water in the gas, the variation of water in the gas is quite large, and the heat of formation of water is relatively large. Therefore, in the combustion gas, the compound heat release of H_2O will transfer a large amount of heat to the wall, thus increasing the proportion of diffused heat flux.

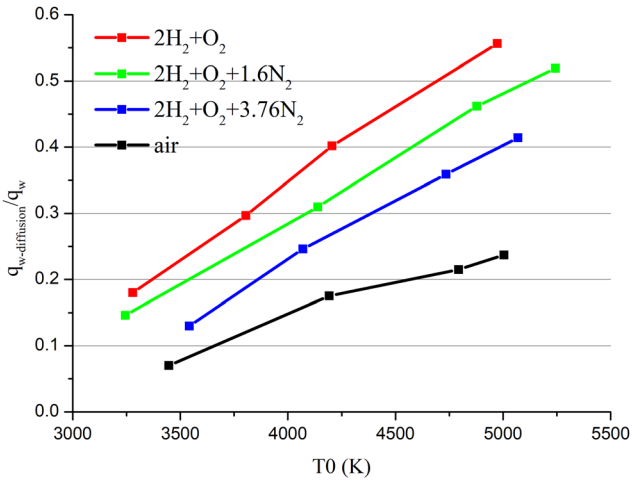

FIG. 14. Proportion of diffusion heat flux at the stagnation point.

For air, we have accurate theoretical formulas to calculate the stagnation point heat flux, such as the famous Fay–Riddell stagnation point heat flux formula,[22] which has long been experimentally verified. Research according to the requirement of the engineering design of the Fay–Riddell formula was improved, and it is concluded that the De Filippis–Serpico formula is a semi-empirical formula (10),[31] but this formula applies only to air. As a result of the gas and air in the vast difference between the transport properties and chemical reactions, directly using this formula to calculate the stagnation point heat flux of an object in a high-speed combustion gas flow will produce a large error, as shown in Fig. 15. The principle of aerodynamic heating of combustion gas and air is the same, both of which are caused by thermal conduction and mass diffusion. Therefore, the structure of the De Filippis–Serpico formula remains unchanged, and what needs to be modified is the coefficient,

$$q_{w0} = 2.75 \times 10^{-5} \cdot \sqrt{\frac{P_{02}}{R_n}} \cdot H_0^{1.17}. \tag{10}$$

For the convenience of analysis, the De Filippis–Serpico formula is transformed into a linear formula, as shown in the following equation, by deformation:

$$\ln\left(\frac{q_{w0}}{\left(\frac{P_{02}}{R_n}\right)^{-\frac{1}{2}}}\right) = \ln\left(2.75 \times 10^{-5}\right) + 1.17H_0, \tag{11}$$

where q_{w0} is the heat flux of the stagnation point, P_{02} is the pressure of the stagnation point, R_n is the radius of the sphere, and H_0 is the total enthalpy of the combustion gas.

Assuming that the formula of the heat flux at the stagnation point of the sphere is heated by combustion gas is shown in the following equation:

$$\ln\left(\frac{q_{w0}}{\left(\frac{P_{02}}{R_n}\right)^{-\frac{1}{2}}}\right) = k + n \cdot H_0, \tag{12}$$

where K is the heat flux coefficient and N is the enthalpy difference index.

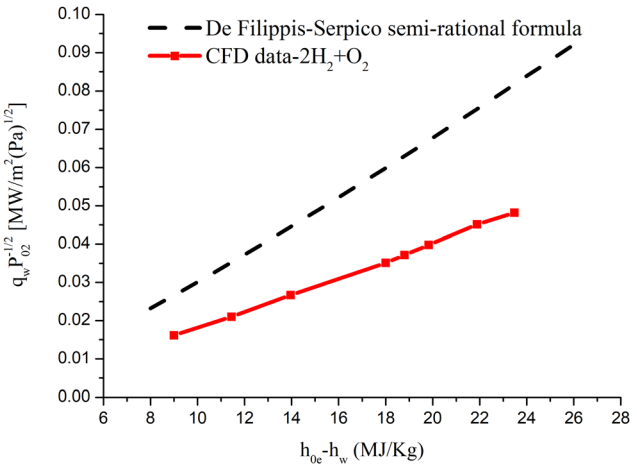

FIG. 15. De Filippis–Serpico formula and the CFD results.

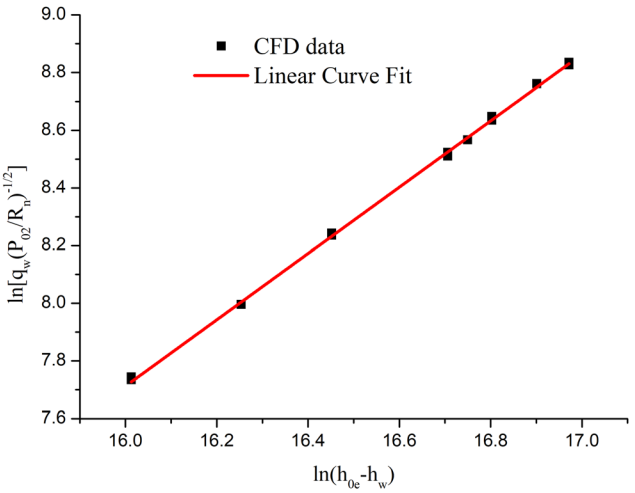

FIG. 16. Heat flux of the stationary point fitting curve.

The complexity of the gas aerodynamic heating also lies in the variable composition of the gas. For various types of engines fueled by H_2 and O_2, the H_2 and O_2 ratio depends on the specific situation. In order to simplify the problem, the stagnation point the heat flux of the sphere aerodynamic heating by hydrogen and oxygen equivalent ratio fuel is first studied. When the sphere is heated by high-speed air, the wall enthalpy is low, which is small compared with the total enthalpy, and can be ignored in general. However, if the sphere is heated by high-speed H_2 and O_2 combustion gas, under the condition of catalytic wall, all unreacted gases and dissociated gases at the wall react to generate H_2O and release a large amount of thermal. In this case, the wall enthalpy is not negligible compared with the total enthalpy of the incoming flow. Therefore, when the De Filippis–Serpico formula is modified, the wall enthalpy term is added, i.e., H_0 is written as $(H_0–H_w)$.

Taking the high-performance hydrogen–oxygen rocket engine as an example, the total temperature of the combustion chamber is usually 3000–4500 K, and the heat flux value at the stagnation point of the aerodynamic heating of spheres with different radii by the combustion gas with a H_2 and O_2 equivalent ratio is calculated within this temperature range. After sorting out the calculated results and using the least squares method, the slope is 1.15 and the intercept is −10.69 (Fig. 16). The heat flux semi-empirical formula of the stagnation point of the aerodynamic heating of the sphere by combustion gas with H_2 and O_2 equivalent ratio was obtained, as shown in the following equations:

$$q_{w0} = 2.2786 \times 10^{-5} \cdot \sqrt{\frac{P_{02}}{R_n}}(H_0 - H_w)^{1.15}, \tag{13}$$

$$H_w = \sum C_i h_{Di}. \tag{14}$$

V. CONCLUSIONS

In this paper, the flow and aerodynamic heating characteristics of high-speed hydrogen and oxygen combustion gas are studied by calculation and experiment.

First, the uniformity of the tunnel flow field is tested and compared with the numerical results. It is demonstrated that the high-speed hydrogen and oxygen combustion gas flow generated by the JF-14 high

temperature combustion gas tunnel is stable and uniform. The aerodynamic heating of the sphere by combustion gas with different hydrogen, oxygen, and nitrogen contents was also studied experimentally and numerically. The accuracy of the numerical calculation was confirmed by the comparison of experimental and calculation data.

Then, the flow of air and combustion gas with different hydrogen, oxygen, and nitrogen contents in the nozzle at the same total temperature and pressure is calculated. For combustion gas, in the process of flow in the spreading section of the nozzle, although the change of the component concentration is small, there is still a change, and with an increase in the hydrogen content, the change increases. Since this process is a compound exothermic process, the temperature, pressure, and speed of the combustion gas flow in the nozzle are higher than those of air but the Mach number is slightly lower.

When the air and combustion gas at the same total temperature (3838 K) and pressure (15.5 atm) expand and accelerate to supersonic velocity through the Laval nozzle and then act on the sphere with a radius of 20 mm, a bow shock wave will be formed on the windward side of the sphere. The high-temperature environment after the shock wave dissociates into a large number of combustion products, so more heat is absorbed, the temperature is significantly reduced, and the thermal conductivity coefficient of the combustion gas is concurrently reduced. Under the condition of noncatalytic wall, the wall heat flow is lower than that calculated by freezing flow. The wall heat flux heated by combustion gas is significantly greater than that of air and the wall heat flux gradually increases with an increase in hydrogen and oxygen content. Compared with air, the catalysis wall has a greater influence on the heat flux of the wall heated by combustion gas, and the heat flux of the sphere heated by a high-speed equivalent ratio of hydrogen and oxygen combustion gas, when the wall is catalytic, the heat flux is nearly twice as large as that of the noncatalytic wall. The results show that the stainless-steel shows partial catalysis for air and complete catalysis for the hydrogen and oxygen combustion gas. The active chemical reaction in the combustion gas intensifies the aerodynamic heating of the object. For the structures heated by the high-speed hydrogen and oxygen combustion gas, more reliable thermal protection measures should be taken.

Finally, through the analysis of a large amount of data, a semi-empirical formula for the heat flux of the stagnation point heated by a high-speed hydrogen and oxygen equivalent ratio combustion gas is obtained [Eqs. (13) and (14)].

DATA AVAILABILITY

The data that support the findings of this study are available from the corresponding author upon reasonable request.

REFERENCES

[1]G. P. Sutton, *History of Liquid Propellant Rocket Engines* (AIAA, Reston, VA, 2006), Chap. 3.
[2]G. P. Sutton and O. Biblarz, *Rocket Propulsion Elements* (John Wiley & Sons, New York, 2016).
[3]D. R. Bartz, "A simple equation for rapid estimation of rocket nozzle convective heat transfer coefficients," J. Jet Propul. **27**, 49–51 (1957).
[4]S. Ludescher and H. Olivier, "Experimental investigations of film cooling in a nozzle under rocket-engine-like flow conditions," AIAA J. **57**(3), 1172–1183 (2019).
[5]M. A. DeRidder and W. E. Anderson, "Heat flux and pressure profiles in a oxygen/hydrogen multielement rocket combustor," J. Propul. Power **26**(4), 696–705 (2010).
[6]P. Nikolaos and P. Lukas, "Wall heat flux evaluation in regeneratively cooled rocket thrust chambers," J. Thermophys. Heat Transfer **35**(1), 127–141 (2021).
[7]N. Perakis, D. Rahn, O. J. Haidn, and D. Eiringhaus, "Heat transfer and combustion simulation of seven-element O_2/CH_4 rocket combustor," J. Propul. Power **35**(6), 1080–1097 (2019).
[8]M. N. Ozisik, *Inverse Heat Transfer: Fundamentals and Applications* (CRC Press, Boca Raton, FL, 2000), Chap. 2.
[9]C.-H. Huang and C.-T. Lee, "An inverse problem to estimate simultaneously six internal heat fluxes for a square combustion chamber," Int. J. Therm. Sci. **88**, 59–76 (2015).
[10]N. Perakis, J. Strauß, and O. J. Haidn, "Heat flux evaluation in a multi-element CH_4/O_2 rocket combustor using an inverse heat transfer method," Int. J. Heat Mass Transfer **142**, 118425 (2019).
[11]J. Haemisch, D. Suslov, and M. Oschwald, "Experimental analysis of heat transfer deterioration and pseudoboiling phenomena in a methane cooled combustion chamber at real conditions," AIAA Paper No. 2018-4943 (2018).
[12]N. Perakis and O. J. Haidn, "Inverse heat transfer method applied to capacitively cooled rocket thrust chambers," Int. J. Heat Mass Transfer **131**, 150–166 (2019).
[13]P. Narsai and E. Momanyi,"Indirect heat flux measurements at the nozzle throat of a hybrid rocket motor," in 51st AIAA/SAE/ASEE Joint Propulsion Conference (2015).
[14]B. Betti, D. Bianchi, F. Nasuti, and E. Martelli, "Chemical reaction effects on heat loads of CH_4/O_2 and H_2/O_2 rockets," AIAA J. **54**(5), 1693–1703 (2016).
[15]D. Suslov *et al.*, "Experimental investigation and CFD-simulation of the cooling in an O_2-CH_4 subscale combustion chamber," in Space Propulsion Conference (2012).
[16]N. Perakis and O. J. Haidn, "Wall heat transfer prediction in CH_4/O_2 and H_2/O_2 rocket thrust chambers using a non-adiabatic flamelet model," Acta Astronaut. **174**, 254–269 (2020).
[17]N. Peters, "Laminar flamelet concepts in turbulent combustion," in *Symposium (International) on Combustion* (Elsevier, 1988), Vol. 21, pp. 1231–1250.
[18]N. Peters, *Turbulent Combustion* (Cambridge University Press, Cambridge, 2000).
[19]J. Warnatz, in *Combustion Chemistry*, edited by W. C. Gardiner, Jr. (Springer, New York, 1984).
[20]M. Frenklach and J. Warnatz, "Detailed modeling of PAH profiles in a sooting low-pressure acetylene flame," Combust. Sci. Technol. **51**, 265 (1987).
[21]M. F. Romig, "Stagnation point heat transfer for hypersonic flow," J. Jet Propul. **26**(12), 1098–1101 (1956).
[22]J. A. Fay and F. R. Riddell, "Theory of stagnation point heat transfer in dissociated air," J. Aerosp. Sci. **25**(2), 73–85 (1958).
[23]N. H. Kemp, R. H. Rose, and R. W. Detra, "Laminar heat transfer around blunt bodies in dissociated air," J. Aerosp. Sci. **26**(7), 421–430 (1959).
[24]C. G. Miller, "Experimental and predicted heating distributions for bionics at incidence in air at Mach 10," Report No. NASA-TP-2334 (1984).
[25]J. P. Li, S. Z. Zhang, J. P. Yu *et al.*, "A detonation tunnel with high temperature burnt gas as test medium," Phys. Gases **3**(6), 1–8 (2018).
[26]H. R. Yu, B. Esser, M. Lenartz, and H. Groenig, "Gaseous detonation driver for a shock tunnel," Shock Waves **2**(4), 245–254 (1992).
[27]Z. L. Jiang, J. P. Li, W. Zhao, Y. F. Liu, and H. Yu, "Investigating into techniques for extending the test-duration of detonation-driven shock tunnels," Chin. J. Theor. Appl. Mech. **44**(5), 824–831 (2012).
[28]J. Li, H. Chen, and H. Yu, "A chemical shock tube driven by detonation," Shock Waves **22**(4), 351–362 (2012).
[29]G. J. Sharpe, "Transverse waves in numerical simulations of cellular detonations," J. Fluid Mech. **447**(1), 31–51 (2001).
[30]W. C. Reynolds, *The Element Potential Method for Chemical Equilibrium Analysis: Implementation in the Interactive Program STANJAN, Version3* (Mechanical Engineering Department, Stanford University, 1986).
[31]F. De Filippis, R. Savino, and A. Martucci, "Numerical-experimental correlation of stagnation point heat flux in high enthalpy hypersonic wind tunnel," in *AIAA/CIRA 13th International Space Planes and Hypersonics Systems and Technologies Conference* (AIAA, 2005), pp. 715–726.